Title

Effective physical properties of cell–cell interaction explain basic structural units of three-dimensional morphogenesis

Short title

Effective potential of cell–cell interaction on morphogenesis

Authors

Hiroshi Koyama[1,2,*], Hisashi Okumura[2,3,4], Atsushi M. Ito[5], Tetsuhisa Otani[2,6], Kazuyuki Nakamura[7,8], Kagayaki Kato[2,9,10], and Toshihiko Fujimori[1,2]

[1]Division of Embryology, National Institute for Basic Biology, 5-1 Higashiyama, Myodaiji, Okazaki, Aichi 444-8787, Japan

[2]SOKENDAI (The Graduate University for Advanced Studies), Hayama, Kanagawa 240-0193, Japan

[3]Biomolecular Dynamics Simulation Group, Exploratory Research Center on Life and Living Systems (ExCELLS), National Institutes of Natural Sciences, 5-1 Higashiyama, Myodaiji, Okazaki, Aichi 444-8787, Japan

[4]Institute for Molecular Science, National Institutes of Natural Sciences, 5-1 Higashiyama, Myodaiji, Okazaki, Aichi 444-8787, Japan

[5]Department of Helical Plasma Research, National Institute for Fusion Science, National Institutes of Natural Sciences, 322-6 Oroshi-cho, Toki, Gifu 509-5292, Japan

[6]Division of Cell Structure, National Institute for Physiological Sciences, 5-1 Higashiyama, Myodaiji, Okazaki, Aichi 444-8787, Japan

[7]School of Interdisciplinary Mathematical Sciences, Meiji University, 4-21-1 Nakano, Nakano-ku, Tokyo 164-8525, Japan

[8]JST, PRESTO, 4-1-8 Honcho, Kawaguchi, Saitama 332-0012, Japan

[9]Bioimage Informatics Group, Exploratory Research Center on Life and Living Systems (ExCELLS), National Institutes of Natural Sciences, 38 Nishigonaka, Myodaiji, Okazaki, Aichi 444-8585, Japan

[10]Laboratory of biological diversity, National Institute for Basic Biology, 38 Nishigonaka, Myodaiji, Okazaki, Aichi 444-8585, Japan

*Correspondence: Hiroshi Koyama

Division of Embryology, National Institute for Basic Biology, 5-1 Higashiyama, Myodaiji, Okazaki, Aichi 444-8787, Japan

Phone: +81 564 59 5862,

hkoyama@nibb.ac.jp.

Keywords

morphological diversity, mechanics, multi-cellular system, effective potential of cell–cell interaction, early embryogenesis

Abstract

Physical properties of cell–cell interactions have been suggested to be critical for the emergence of diverse three-dimensional morphologies of multicellular organisms. Their direct evaluation in living systems, however, has been difficult due to technical limitations. In this study, we developed a novel framework for analyzing and modeling the physical properties of cell–cell interactions. First, by analogy to molecular and colloidal sciences, cells were assumed to be particles, and the effective forces and potentials of cell–cell interactions were statistically inferred from live imaging data. Next, the physical features of the potentials were analyzed. Finally, computational simulations based on these potentials were performed to test whether these potentials can reproduce the original morphologies. Our results from various systems, including Madin-Darby canine kidney (MDCK) cells, *C.elegans* early embryos, and mouse blastocysts, suggest that the method can accurately capture the diverse three-dimensional morphologies. Importantly, energy barriers were predicted to exist at the distant regions of the interactions, and this physical property was essential for formation of cavities, tubes, cups, and two-dimensional sheets. Collectively, these structures constitute basic structural units observed during morphogenesis and organogenesis. We propose that effective potentials of cell–cell interactions are

parameters that can be measured from living organisms, and represent a fundamental principle underlying the emergence of diverse three-dimensional morphogenesis.

Introduction

The physical properties of interactions between objects are among the most fundamental parameters of various physical, chemical, and biological phenomena at a wide range of spatial scales in the molecular, colloidal, cellular, and astrophysical sciences. Interactions among particulate matter such as ions, molecules, and colloids are primarily mediated by electromagnetic forces, and the properties of these interactions, including attractive and repulsive forces, substantially affect the dynamics and stability of systems [1,2]. In multi-cellular living systems, various three-dimensional morphologies are observed. The emergence of these diverse morphologies is thought to be primarily dependent on the physical properties of the constituent cells. In particular, mechanical properties of cell–cell interactions are involved in morphogenetic events such as epithelial cell movement and cell sorting [3–7]. However, the physical basis of morphogenesis, which gives rise to a variety of structures, remains to be elucidated, and it is not yet known whether any unifying principle can explain the morphological diversity of organs and tissues.

The properties of cell–cell interactions are regulated by various factors. In epithelial cells, whose shapes are typically columnar polygons, cell–cell adhesion energy is controlled by cadherin family proteins (Fig. S1A-i and B) [3,4,8], whereas

actomyosin proteins counteract adhesion through the indirect effect of cell surface tension (Fig. S1A-i and B) [9,10]. By contrast, in mesenchymal cells, which are unstructured shapes, in addition to cadherins, cell–cell interactions are regulated by indirect interactions through extracellular matrix (Fig.S1A-i) [11–13]. Therefore, cell–cell interactions entail many parameters determined by various proteins and cellular processes, resulting in very complex physics with many degrees of freedom (Fig.S1A-i). To elucidate the principles underlying morphological diversity, it is essential to investigate how the integrated effects of many parameters can be described as simple mesoscale parameters (Fig. S1A-ii).

In non-living materials such as ions, molecules, and colloids, interactions among particulate matter are determined by electron clouds, which have complex shapes, and by the shapes of the particles themselves (Fig. S1A-iii) [14]. The potentials of particle–particle interactions are widely recognized as mesoscale parameters. Here, potential energies are defined as a function of particle–particle distance, e.g., the Lenard–Jones potential (Fig. S1A-iv). Effective potentials of interaction have been widely measured or inferred by various methods, including a previous study by our group [1,2,15], and these potentials are used to perform molecular dynamics simulations [16]. The potential of cell–cell interaction is also conceptually well recognized, and has been

used in theoretical studies (Fig. 1E and S1A-ii) [11,17–25]. Although interaction forces in isolated cells have been measured [6,26], they have neither been measured nor inferred in more complex multi-cellular systems, which differ from isolated cells as a consequence of environmental effects. Furthermore, whether the potential of cell–cell interaction alone is effective and sufficient to explain diverse three-dimensional morphologies has not been evaluated.

In this study, by analogy to non-living materials (Fig. 1), we developed a method for statistically inferring the effective potential of cell–cell interactions using nuclear tracking data from live imaging, which are relatively easy to obtain. We successfully applied this method to relatively small multi-cellular systems (4–350 cells) including mouse pre-implantation embryos and early embryos of the nematode *Caenorhabditis elegans*. Further theoretical analyses suggested that effective potential represents a unifying principle capable of explaining basic structural units during three-dimensional morphogenesis; these basic structures are formed prior to the morphogenesis of complex tissue structures. We describe the differences in these potentials between living and non-living materials, as well as among biological species. Moreover, we discuss the usefulness of our sequential method for establishing *in situ* mechanical maps and connecting model parameters to *in vivo* parameters including the

activities of gene products.

Mathematical model & methods

Overview of strategy for inferring effective potentials/forces of cell–cell interaction

To measure or infer the effective potentials or forces of cell–cell interactions *in vivo*, we developed a particle-based cell model in which attractive or repulsive forces are exerted between each pair of cells (Fig. 1A and B). Simultaneously, we obtained time series of three-dimensional cell positions from confocal microscopic images (Fig. 1C) and statistically inferred the effective forces of cell–cell interactions by systematically searching for force values that could reproduce the cell movements observed *in vivo* (Fig. 1D). To validate the method, we utilized artificial cell movement data generated by performing simulations under given potentials of cell–cell interactions, and confirmed that the inferred forces were consistent with the given-potentials. The details of each part of the analysis are explained in the following sections.

Particle-based cell models

In our model, cells are assumed as particles, regardless of type or origin (e.g., epithelial, mesenchymal, or blastomere cells) (Fig. 1A and S1A). Particles interact with each other and attractive or repulsive forces (F_i) are assumed (Fig. 1B), where i is an identifier for particle–particle interactions. Defining the range of particle–particle

interaction distances is essential for performing simulations. In particle-based models such as those used for molecular dynamics simulations [27,28], a cut-off distance for particle–particle interactions is typically set to exclude non-effective interactions, where the interaction forces are sufficiently small to be negligible. On the other hand, a cell is able to interact not only directly with the cells it physically contacts, but also indirectly with non-contacting cells through the extracellular matrix (Fig. S1A-i) [11–13]. Furthermore, some cells form protrusive long structures in order to interact with distant cells (Fig. S1A-i) [29,30]. These properties depend on tissue and cell type. Because it is difficult to detect and identify all of these interactions by microscopic imaging, it is essentially impossible to strictly define a physical interaction distance or cut-off distance in multi-cellular systems. Therefore, in this study, we assumed that effective interaction distances were ~3-fold larger than the diameters of “cell bodies”, i.e., the non-process portions of cells, (Fig. S2A-i). Importantly, this cut-off distance did not substantially affect the results of inference of effective forces as shown later (Fig. S7A and SI, Section 3-3-4). The diameters of cell bodies were estimated using the Voronoi tessellation (Fig. S2A-i and SI, Section 3-3-1). In our framework, the pair-wise interaction forces were considered, and neither cell polarities (apico-basal and planar cell polarities) nor the effect of multibody particle–particle interactions were directly

considered, which can be implemented by assuming a cell composed of two particles or a Voronoi-based cell [31–35]. We did not assume persistent random walks which are originated from cellular traction forces on substrates [32,36], because we focused on cellular systems with no attachment to substrates.

The equation of particle motions is defined below. In cellular-level phenomena, viscous drag force or frictional force provided by the surrounding medium or tissue is dominant, as expected from the Reynolds number; consequently, the inertial force is negligible in general [5,11,13,37,38], in contrast to the situations for molecular motion. The forces in such a system can be assumed to be correlated with the velocities of the objects [5,13,24,25,31]. Thus, the velocity (V_p) of a particle is calculated by the net force (F_p) exerted on the particle as follows:

$$V_p = F_p / \gamma \qquad \text{(Eq. 1)},$$

where p is an identifier for particles and γ is the coefficient of viscous drag and frictional forces. F_p is the summation of F_i: $F_p = \sum_{i=1}^{I} \delta(p) F_i$, where I is the total number of interactions, and in the case that the ith interaction is formed with the pth particle, $\delta(p)$ is 1, otherwise $\delta(p)$ is 0 (Fig. 1B). Thermal fluctuations or noises of cellular activities are included as follows:

$$V_p = F_p / \gamma + \zeta, \qquad \text{(Eq. 2)},$$

where ζ is the fluctuation or noise. This is the equation of the motion of each particle. Because it is difficult to experimentally measure the value of γ and its spatiotemporal distributions as discussed in SI (Section 3-5-2), we assumed the simplest situation, i.e., γ is constant (=1.0). In addition, ζ was assumed to be negligible (=0). The influence of these assumptions on simulation results is discussed in SI (Section 3-4, 3-5-2, and 6).

Data acquisition of time series of cell positions

To define cell positions, we focused on nuclei, because they are most easily imaged by microscopy (Fig. 1C). Although centroids of cells are candidate alternatives for cell positions, it is challenging to obtain centroid positions in three-dimensional tissues. Therefore, because our method uses nuclear positions, we expect that it could be used in a wide range of tissues and organisms. By utilizing confocal microscopy or other optical microscopy methods, nuclei labeled with fluorescence markers such as genetically encoded histone-GFP (green fluorescent protein) and chemical reagents such as Hoechst can be three-dimensionally imaged. In fact, nuclear detection followed by temporal tracking has been performed in a wide range of organisms from *C. elegans* to mammals, and these data are accumulating [39–43]. We utilized publicly available nuclear tracking data of a developing embryo of *C. elegans* [39]; nuclear tracking data of

developing mouse embryos and MDCK cultured cells were obtained in this study (SI, Section 1, 7, and 10 with text data). Procedures for tracking cell division are described in SI (Section 2) and Figure S2B.

Development of method for inferring effective potentials/forces of cell-cell interaction

In the case of ions, molecules, etc., radial distribution functions are often measured and used to infer the effective potentials of their interactions [1,2]. Although this method is simple and applicable to thermodynamically equilibrium systems, it is not suitable for non-equilibrium systems, including morphogenetic events. To infer the effective potentials of non-equilibrium systems, we fitted the particle-based cell model to the time series of nuclear positions in the spirit of data assimilation, in which an inverse problem is solved using a simulation model [44,45]. Because γ was assumed to be constant in Equation 2, we can only infer relative, but not absolute, values of effective forces. Through repeated cycles of simulations of the model, we systematically searched for the values of the effective forces that minimized the differences between the particle positions in the simulations and the *in vivo* nuclear positions (Fig. 1, and S2C). The differences (G_{xyz}) to be minimized are defined as follows (SI, Section 3-1 and 3-2).

$$G_{xyz} = \sum_{t=1}^{T} \sum_{p=1}^{P(t)} \frac{\left\{x_p(t) - x_p^{\mathrm{ref}}(t)\right\}^2 + \left\{y_p(t) - y_p^{\mathrm{ref}}(t)\right\}^2 + \left\{z_p(t) - z_p^{\mathrm{ref}}(t)\right\}^2}{\Delta t}$$

(Eq. 3)

Here, p is an identifier for particles, t is an identifier for time frames, and Δt is the time interval between the time frames. The x, y, and z coordinates of the pth particle obtained from microscopic images are x_p^{ref}, y_p^{ref}, and z_p^{ref}; ref means reference (Fig. S2C). The coordinates during the repeated cycles of simulations are x_p, y_p, and z_p. The effective forces were inferred for each cell–cell pair for each time frame (Fig. S2B and C).

Because a cut-off distance was defined before the inference, as mentioned above in the model description section, consistency between inferred effective forces and the cut-off distance should be maintained. Considering a cut-off distance is equivalent to making an assumption that the effective forces are zero at greater distances (Fig. S2A-ii). Therefore, the absolute values of the inferred effective forces at distances shorter than the cut-off distance should approach zero near the cut-off distance (Fig. S2A-ii). Otherwise, a discontinuity in the relationship between the forces and the particle–particle distances would be produced at the cut-off distance, which is not physically reasonable (Fig. S2A-ii), because the values of the effective forces would change abruptly at the cut-off distance. To achieve the correct profile of the effective forces mentioned above, we assumed that a constraint for force values was incorporated

in the function to be minimized during the inference. We defined an additional cost g_{F_0} for the minimization, as follows:

$$g_{F_0} = \sum_{t=1}^{T} \sum_{i=1}^{I(t)} \psi(D_i) F_i^2 \Delta t \qquad \text{(Eq. 4)}$$

Here i is the ID of particle–particle interactions, F_i is the effective force of the ith interaction, and D_i is the distance of the ith interaction obtained from the microscopic imaging data. $\Psi(D_i)$ defines the D_i-dependent weight of the cost, and was an exponential function of D_i, set to be extremely large around the cut-off distance (Fig. S2A-iii and SI, Section 3-3-2 to 3-3-4). If $\Psi(D_i)$ was set to be constant, inferred effective forces became far from zero even at long distant regions as shown later. Distance-dependent constraints other than Equation 4 were assessed, but they did not improve the inference results (SI, Section 3-3-5). By defining the summation of the Equations 3 and 4 as the function to be minimized as follows,

$$G = G_{xyz} + G_{F_0} \quad (G_{F_0} = \omega_{F_0} g_{F_0}) \qquad \text{(Eq. 5)},$$

the inferred effective forces approached zero around the cut-off distance. To set the value of the coefficient (ω_{F_0}) of the second term, we defined accuracy of particle positions calculated from the first term, as shown in SI (Section 3-3-3). The value of the coefficient was set so that the particle positions in the simulations exhibited ~98% consistency with the *in vivo* nuclear positions. In the absence of the second term, this

minimization problem exhibited indefiniteness (i.e., a unique solution could not be determined) and over-fitting also occurred. The second term is considered as the prior in the Bayesian inference, and, in general, a unique solution could be ensured by introducing such a prior [44]. Detailed procedures are described in SI (Section 3-4).

Validation of inference method

To determine whether our method can correctly infer effective forces, we first applied it to artificial data generated under given potentials of particle–particle interactions, and examined whether the inferred effective forces were consistent with the given potentials (Fig. S3A). We tried the Lenard–Jones (LJ) potential, well-known as the potential between atom–atom interactions, as a test case of the given potentials. By performing particle simulations under the LJ potentials with various scales of forces, we obtained time series of the particle positions (Fig. S3A, SI, Section 3-3-4-1, and Movie S1A). Then, we applied the inference method to the time series, yielding effective forces for each pair of particles for each time frame (Fig. S3B). The inferred effective forces were plotted against particle–particle distance (Fig. S2D, S3C, and SI, Section 4). The plots were almost distributed around the distance–force curve calculated from the LJ potentials. By averaging the plots for each shallow bin of distances, we also

obtained distance–force (DF) curves, which were consistent with the curves from the LJ potentials (Fig. S3C). Importantly, the scales of the forces were also correctly inferred (Fig. S3E). Furthermore, we tried other potentials generated by freehand drawing, called "FH" potentials in this study, as an alternative to the LJ potentials (Fig. S3A and Movie S1B). The FH potentials were chosen because the simulation outcomes under the FH potentials differ from those under the LJ potentials as shown later (Fig. S8). The inferred DF curves were almost consistent with the given potentials bearing various force scales (Fig. S3C and E). An optimal profile of $\Psi(D_i)$ was defined using these potentials (Fig. S3D and SI, Section 3-3-4-2); additionally, the inferred DF curves under a constant value of $\Psi(D_i)$ were not consistent with the given potentials (Fig. S3D, α=1). Conversely, we also tried using time series of random–walk simulations as negative controls (Fig. S3A and Movie S1C). The plots of the inferred effective forces against distances were widely distributed, and the DF curves generated from the plots by averaging were zigzag and disorganized (Fig. S3C and E). These results indicate that our method can correctly infer DF curves.

Validation of inference method by using non-adhesive cells

Before applying our inference method to three-dimensional multi-cellular

systems, we performed an additional negative control experiment using two-dimensionally cultured cells that exhibit negligible cell–cell interactions. Because cultured MDCK cells adhere to each other via cadherin proteins, cadherin-deficient mutant cells experience almost no adhesion. We knocked out cadherin function (E-cadherin and cadherin-6 in the case of MDCK cells) by knockout of the gene encoding α-catenin, an essential regulator of the two cadherins [46]. The nuclei of the living cells were labeled by Hoechst 33342, and time-lapse microscopic imaging was performed (Movie S2A). α-catenin knockout (KO) cells moved on cultured dishes because they have a self-propelled activity originated from their traction forces on substrates. In comparison with wild-type MDCK cells (Movie S2B), the movements of the mutant cells were less coordinated, resulting in random walk–like movements. We used these cells as a model with random walk–like movements. We tracked the nuclei by image processing and obtained time series of nuclear positions. Our inference method was applied to these time series, and the inferred effective forces were plotted against distance. The dimensions of the forces were arbitrary units (A.U.); 1 [A.U.] of the force can move a particle with a velocity of 1μm/min. In contrast to wild-type MDCK cells which had organized DF curves (Fig. S4B), the inferred effective forces of α-catenin KO cells were widely distributed, similar to those obtained from random-walk

simulations (Fig. S4A). The DF curves obtained by averaging were also disorganized (Fig. S4A). This result supports the idea that our method is accurate enough to infer intercellular forces in multi-cellular systems.

Results

Inference of effective forces in C. elegans early embryo

After confirming that our method can correctly infer effective forces between particle–particle interactions, including those in two-dimensional cellular systems, we next investigated whether it could obtain effective forces in three-dimensional systems. The nematode *C. elegans* has well-defined embryogenesis: cell movements in early embryos are almost identical among different individuals, and the time series of nuclear positions have been reported previously [39]. In addition, the spatiotemporal patterns of cell differentiation are absolutely the same: cell lineage and cell fate are invariant. During early *C. elegans* embryogenesis, a fertilized egg (i.e., one cell) repeatedly undergoes cell division and cell differentiation, ultimately forming an ovoid embryo containing ~350 cells (Fig. S5A and Movie S3A). The cells become smaller through cell division [47], and the total volume of the embryo remains constant because the embryo is packed into a stiff egg shell. Thus, the volume of each cell is reduced by a factor of 350

relative to the original egg, meaning that cell diameter is reduced by a factor of 7. Because particle diameter is approximately reflected on a DF curve as the distance with force = 0 (Fig. S2D) corresponding to the minimum of the potential, we expected that inferred DF curves should be gradually shifted to the left side of the distance–force graph throughout embryogenesis.

Figure 2A is a snapshot that shows nuclear positions and inferred effective forces in the embryo; the temporal change is also visualized (Fig. S5B and Movie S3B), where dynamic changes in the effective forces were observed. Importantly, almost identical values of the effective forces were obtained from different initial values during the minimization process of Equation 5 (Fig. 2B, S7A, and SI, Section 3-4), suggesting that our inference problem may have a unique solution. Moreover, the cut-off distance did not substantially affect the values of the inferred effective forces (Fig. S7A and SI, Section 3-3-4). To investigate whether DF curves change during the embryogenesis, we divided the whole embryogenesis into segments containing different time frames, and plotted the inferred forces against the distances for each segment (Fig. 2C and S5C, time frame = 16–55, 36–75, 76–115, 116–155, and 156–195). The plots were widely distributed in all the segments, but the DF curves generated by averaging in each shallow bin of the distances exhibited organized patterns. This was in striking contrast

to the results of the random-walk simulations and the α-catenin mutant cells. All of the DF curves had very similar profiles: repulsive and attractive forces were detected around the core of the cells and longer interaction distances, respectively (Fig. 2D). The repulsive forces are likely to be derived from the volume effect of the cells, and the attractive forces might be derived from cell-cell adhesion. These patterns are typical in various non-living particle–particle interactions such as atoms and molecules, whose potentials are given by the LJ potential, etc. (Fig. S3A). We also calculated the distance–potential (DP) curves by integrating the force values (Fig. S2D and SI, Section 4). Importantly, the distances in the minimum of the effective potentials were gradually shifted toward the left side (Fig. 2D), as we had expected (Fig. 2E), indicating that the inferred effective potentials were consistent with the reduction in cell volume during embryogenesis (Fig. 2E). Taken together, the patterns of the DP curves seem to be physically reasonable. In addition, the wide distributions of the plots may originate in biological properties, including the intrinsic heterogeneity of cells and/or experimental or methodological errors during detection of cell centers or the inferring process, as discussed in SI (Section 3-5).

Effect of inferred distance–force curves on C.elegans embryonic morphologies

The inferred DF curves for *C. elegans* embryogenesis seem to be reasonable. However, one concern may be that the averaged DF curves are oversimplification, given the broad distribution of the effective force, as discussed later. This prompted us to further investigate whether the simple DF curves can explain embryonic morphologies. Because the dynamics of all cells during embryogenesis are very complicated, largely due to the repeated cell division and cell differentiation, we focused on a few typical features of the morphologies: aggregated cells and the ovoid embryo shape.

We performed simulations based on the particle-based cell model by considering the DF curves, and investigated whether aggregated states with ovoid shapes were stable. As in systems composed of larger colloidal particles, multi-cellular systems are usually in or near metastable states corresponding to local minima, or under non-equilibrium states; therefore, our focus was not limited to thermodynamic equilibrium states corresponding to global minima. To find stable states under the DF curves, we performed simulations starting from various initial configurations of the particles, and the systems were relaxed with no fluctuations ($\zeta = 0$). When we used the DF curves obtained from the *C. elegans* embryos, we observed a tendency for the particles to aggregate with an ovoid or distorted shape (Fig. 5A and S8). Other simulation outcomes were also shown in Figure S8. Thus, aggregated states with ovoid

shapes are one of the stable states under the DF curves. As a control simulation, we utilized the LJ potential, and found that it did not generate an ovoid or spherical shape, but rather a shape similar to its initial configuration (Fig. S8). Moreover, the FH potentials generated a spherical but not ovoid shape, and the outcomes were not significantly affected by the initial configurations (Fig. S8). These results suggest that the inferred effective DF curves are capable of recapitulating the basic morphology of the *C. elegans* embryos.

Inference of effective force in mouse pre-implantation embryos

To further investigate whether effective forces could be obtained in three-dimensional systems, we focused on mouse pre-implantation embryos, including morulae at the 8-cell and compaction stages, as well as blastocysts (Fig. 3A, illustration). These embryos are surrounded by a spherical egg shell–like structure called the zona pellucida, but even if that structure is removed, the embryos maintain their spherical shapes and development normally [48]. In 8-cell stage embryos before compaction, cell–cell adhesion is weak, and individual cells can be easily discerned (Fig. 3A, bright field). In the compaction-stage embryos composed of ~32 cells, cell–cell adhesion becomes stronger due to elevated expression of cadherin proteins on cell membrane, and the cells

are strongly assembled [49]. The surface of the embryo becomes smooth, and the embryonic shape becomes more spherical (Fig. 3A, bright field). In blastocyst-stage embryos composed of >64 cells, an inner cavity is formed, and the embryos expand while maintaining their spherical shape. Trophectoderm (TE) cells form a single–cell-layered structure at the outermost surface of the embryo, whereas the cells of the inner cell mass (ICM) were tightly assembled, forming a cluster (Fig. 3A, illustration). Using confocal microscopy, we performed live imaging of fluorescently labeled nuclei, obtained time series of the nuclear positions (Fig. 3A, Movie S4A-C, and SI, Section 7-1), and then applied the inference method.

Figure 3B shows the snapshots of the inferred effective forces of cell–cell interactions during the three embryonic stages that we examined (Movie S4D–G). The uniqueness of the solutions was confirmed (Fig. S7). We calculated the DF and DP curves in a manner similar to *C. elegans* study described above, and obtained curves for all three stages (Fig. 3C and D). The DF curves derived from the 8-cell and compaction stages had typical profiles, with repulsive and attractive forces detected at short and long interaction distances, respectively (Fig. 3D and S5D). On the other hand, the DF curves derived from the blastocyst stage had an additional repulsive force at long interaction distances, which we refer to as the distant energy barrier, DEB (Fig. 3D,

arrows). Such energy barriers are known in molecular and colloidal sciences, and affect dynamics of the particles [1,2], although they have not been discovered in multi-cellular systems. Together, these results indicate that the profile of DF curves changes during the development. Moreover, the profiles of the DF curves suggest the consistency with previous experimental knowledges as described in Figure S6.

Effect of inferred distance–force curves on mouse embryonic morphologies

We next asked whether the temporally evolved DF curves derived from the mouse embryos were sufficient to explain the key morphological features of the embryos. Using the DF curves, we searched for stable states by an approach similar to the one we used for *C. elegans* embryos. In contrast to the case of *C. elegans* embryos, in which an ovoid shape was generated, the DF curve derived from the compaction stage embryo yielded a spherical shape where particles were aggregated (Fig. 5B and S8). In the case of the 8-cell stage embryo, simulation results were similar to those obtained for the compaction stage, except that the spherical shape seemed to be slightly distorted (Fig. S8). In the case of the blastocyst stage embryo, when aggregated particles were given as initial configurations, the particles gradually scattered and converged to form a spherical structure harboring a cavity at the center (Fig. 5B). The

429 particles often formed clusters, each composed of two to four particles, which
430 resembled the ICM (although the real ICM is composed of several tens of cells). The
431 cavity-bearing shape was a converged state but not a stable state: the distances between
432 the clusters were equivalent to the distance of DEB, meaning that even slight thermal
433 fluctuations or noise from cellular activities would break the structures. It is likely that
434 the gradually expanding structure harboring a cavity reflects a transient state during
435 blastocyst expansion [48]. Thus, we speculate that these simulations recapitulated
436 developmental dynamics rather than stable states. Importantly, when DEB was
437 eliminated from the DF curves, no cavity was generated (Fig. 5B). These results suggest
438 that all of the DF curves from the various embryonic stages are sufficient to explain
439 their different morphologies. The roles, effects, and origin of DEB will be analyzed or
440 discussed below. Later we will also discuss the differences in the DF curves between the
441 two cell populations TE and ICM (Fig. S6). We will also discuss cellular polarities, such
442 as apico-basal and planar cell polarities that were not considered in this study.

443

444 *Inference of effective distance–force curves and their effect on morphology in MDCK*
445 *cyst*

446 The above results led us to hypothesize that DEB of the DF curves plays

essential roles in the morphogenesis of structures harboring cavities. To examine this hypothesis, we focused on another system with a cavity. MDCK cells, derived from dog kidney epithelium, can form cysts containing a cavity when cultured in suspension (Fig. 4A, illustration) or in gels composed of extracellular matrix [50]. To exclude mechanical interactions between the cysts and the external environment, we chose suspension conditions in which a cyst can be assumed to be a mechanically isolated system for which external forces are negligible. We obtained time series of the nuclear positions of the cysts by a procedure similar to the one used for the mouse embryos (Fig. 4A, Movie S5A, and SI, Section 7-2). We then inferred the effective forces and calculated the DF curves (Fig. 4B–D and S5E). The uniqueness of the solutions was confirmed (Fig. S7). Figure 4D shows the DF and DP curves from a MDCK cyst. We found a DEB in the DF curves, implying that a DEB is generally involved in morphogenesis of cavity-bearing structures.

Simulations based on inferred DF curves revealed that, in contrast to the blastocysts, a cavity was stably maintained in MDCK cells even under slight fluctuations (Fig. 5C and S8). On the other hand, when aggregated particles were given as initial configurations, a cavity was not newly formed (Fig. S8). Moreover, the DF curves without the DEB could not maintain the cavity-bearing structure (Fig. 5C).

Taken together, these findings indicated that the DEBs in the blastocyst and the MDCK cyst play roles in the formation and maintenance of a cavity, respectively.

Modeling of distance–force curves

Given our finding that DF curves bearing DEBs are critical for morphogenesis of cavity-bearing structures, we hypothesized that the DF curves represent a rule capable of explaining various morphogenetic events. Moreover, the profiles of the DF curves in Figure 2-4 were quantitatively different each other (Table S1), suggesting the quantitative differences are critical for morphogenesis. To comprehensively understand the effect of the profile of the DF curves on morphogenesis, it is necessary to model the DF curves as a simple mathematical equation. We selected the following equation as described in SI (Section 5):

$$F(D) = \varepsilon(D - D_0)^{-N} \cos\left\{\frac{2\pi(D - D_0)}{\delta}\right\}, \text{ for } D > D_0 \qquad \text{(Eq. 6)}$$

Here, F is the force, D is the distance, and N is the exponent of D, affecting the decay of the DF curves along D (X-axis). D_0 and δ affect the profile of the DF curves as shown in Figure 6A. Specifically, D_0 can transform the DF curves along D, and δ affects the wavelength of the cosine function. By introducing a normalized variable $D_0^* = D_0/(\delta/4)$, we found that the simulation outcomes below became identical under the same value of

D_0^* (data not shown). This enabled us to present simulation outcomes in two-dimensional space (D_0^* and N) in a manner similar to a phase diagram (Fig. 6).

Systematic analyses of the roles of the distal energy barriers

Using the DF curves defined by Equation 6, we systematically investigated what kind of morphologies could be generated or remain stable, and what kind of morphological transformation could be achieved. Here, we tried to identify possible stable states, including metastable states. We set various initial configurations of particles, performed simulations under various DF curves, and then searched for local minimum states. A cavity-bearing structure was set as the initial configuration (Fig. 6B). The simulation outcomes were categorized by their morphologies and plotted on a two-dimensional space (Fig. 6B). Examples of the morphologies and DF curves are also shown. We identified cavity-bearing structures ("cavity" and "cavity with extra particles"), cups, tubes, and lattices / aggregates as possible stable states. Multi-clusters and disorganized morphologies were also generated. Importantly, when the DEBs were eliminated from the DF curves, one of the cavity-bearing structures ("cavity"), cups, or tubes were not generated (Fig. 6C), indicating that the DEBs are essential for the formation or maintenance of these structures.

Next, we tried other initial configurations of particles. A monolayer two-dimensional sheet was applied as the initial configuration (Fig. 6D), and slight positional noise was introduced. The simulation outcomes included spherically aggregated structures, cavity-bearing structures, and two-dimensional sheets (Fig. 6D). In contrast to Figure 6B, the cavity-bearing structures were newly generated even in the absence of the DEBs (Fig. 6E). The monolayer two-dimensional sheets were maintained (Fig. 6D), and this was largely dependent on the DEBs (Fig. 6E). We confirmed that the generated two-dimensional sheets were not broken by slight positional fluctuations (data not shown), indicating that the structures were stable.

These analyses indicated that, by considering the DEBs, the DF curves represent a powerful rule for the formation and maintenance of various three-dimensional structures. Other analyses considering different particle numbers are shown in Figure S9, indicating that the probability of the emergence of tubes, cups, and cavities was affected by the particle numbers. In addition, the structures generated by the particle model included a chain and sorting of multiple cell types (Fig. S9), suggesting that the particle model is applicable to more complicated structures.

Possible transitions among various structures

The results presented above demonstrate that the basic structural units of morphogenesis, including cell aggregates, cavity-bearing structures, cups, tubes, two-dimensional sheets, and sorted cells, can be formed or maintained by the DF curves harboring DEBs. Indeed, these structures are typically observed during embryogenesis and morphogenesis: cell aggregates [20,39,51–56], cavity-bearing structures [50,51,57–59], two-dimensional sheets [20,34,55,60–62], tubes [63–65], and cups [52]. Moreover, transitions among some of these basic structural units are observed. Hence, we next investigated whether modulation of the profiles of the DF curves can induce transitions among these structures. We modulated the profile of the DF curves by modifying the values of the variables in Equation 6. Through trial-and-error of the modulation of the profile, we found that these structures transformed each other as shown in Figure 7 and Movie S6. These results suggest that temporal evolution of the profile of the DF curves can potentially reproduce some developmental processes during embryogenesis and morphogenesis.

Discussion

In this study, we developed a method for statistically inferring effective forces

of cell–cell interactions using nuclear tracking data obtained from microscopic images. We then demonstrated that effective potentials of cell–cell interactions can be extracted from the inferred forces in various living systems. Our findings provide for the first time the experimental quantification of effective potentials, which have been recognized conceptually [11,17]. By considering the effective potentials, we successfully reproduced various three-dimensional structures, including basic structural units observed during embryogenesis, morphogenesis, and organoids. These basic structures lead to the formation of complex tissue structures. For instance, cell aggregates are observed in early embryos in various species and spheroids [20,39,51–56]; cavity-bearing structures in early embryos of various species, organoids, and cystic diseases [50,51,57–59,66]; cell sheets in epithelia and germ layers [20,34,55,60–62]; tubes in tubular organs [63–65]; and cups in retina and murine epiblast [52,67]. These results suggest that the effective potentials alone are sufficient to explain diverse three-dimensional morphologies. Although cell–cell interactions are affected by many parameters including proteins such as cadherins and cellular structures such as actomyosin cytoskeletons (Fig. S1 and S4), we suppose that the effective potentials can be an integrative and unifying mesoscale parameter to explain morphogenetic events. Our goal is to develop a framework for explaining diverse morphogenesis in a minimal model. The model based on effective potential

represents such a framework with few degrees of freedom (Fig. S1A), and this provides a novel paradigm for understanding the morphogenesis of multi-cellular systems and their morphological evolution. We believe that effective potentials and the inference method constitute a powerful approach for exploring principles for diverse morphogenesis.

Profile of effective potentials of cell–cell interaction

We discovered distant energy barriers (DEBs) in the effective potentials obtained from blastocysts and MDCK cysts. These energy barriers contributed significantly to the generation and maintenance of cavity-bearing structures, tubes, and sheets. Such energy barriers are well-known in molecular and colloidal sciences, as mentioned in SI (Section 4-4-1). We speculate the physical interpretation of these energy barriers in cells below. In the case of the blastocysts, the trophectoderm cells form tight junction to seal gaps between the cells and transport liquid from the outside of the embryos to the cavities, resulting in increased hydrostatic pressure, fracturing of the cell-cell contacts of the inner cells, and subsequent expansion of the cavities [68–70]. Therefore, the TE cells push each other through the liquid in the cavities. This indirect mechanical repulsion might be reflected in the DEBs (Fig. S10A). In the case of the

MDCK cysts, tubes, and sheets, these structures are usually composed of epithelial cells, which form single-layered sheets. The MDCK cysts and tubes are curved sheets. In order to maintain a sheet, protrusion of a cell from the sheet and its subsequent approach to non-adjacent cells should be prohibited; otherwise, the cells form an aggregate (Fig. S10B). The DEBs can suppress these processes by providing long-range repulsion between non-adjacent cells (Fig. S10B). Thus, we think that effective potentials represent a unifying principle that could integrate indirect parameters such as hydrostatic pressure outside of cells.

We also analyzed the profiles of the effective potentials in detail by calculating the slopes of the DP curves (Fig. S11 and SI, Section 4-4-2). We found that the cores of the cells during mouse compaction were softer than those of other cells, as well as those of particles bearing the LJ potentials, suggesting that the cells are deformable (Table S1). Moreover, the interactions during the compaction stage range over longer distances (Table S1), consistent with a previous experimental observation that cells during compaction have long filopodia [49], which accelerates assembly of the cells. Thus, these features may explain the spherical assembly of the cells during compaction. Possible contributions of surface shapes and of surface forces of cells to the potentials are discussed in SI (Section 3-5-2).

Potentials of cell–cell interactions have been widely considered in various materials such as active matter including self-migratory cells. In these studies, however, the profiles of the potentials are given artificially, and experimental bases are lacking. For instance, hard- or soft-core, square-well, JKR, and other potentials have been considered [19,20,25,71,72]. Animal and human behaviors can also be modeled as active matter governed by attractive and repulsive interactions [73–76]. Our inference method can be used to obtain the profiles of the potentials in these materials, possibly leading to new finding of the dynamics of these materials. Moreover, the material properties of particulate soft matter can be estimated using inferred effective potentials.

Usefulness, application, and limitation of inference method

As demonstrated here, our inference method is applicable to various tissues and species. This is because our method requires only nuclear tracking data, which is easily acquired through microscopic imaging and subsequent image processing. Although various cellular structures, such as cell membranes, have been imaged, precise segmentation of these structures by image processing is still challenging in three-dimensional situations [77]. On the other hand, nuclei can be labeled genetically or chemically, and they are easily segmented in comparison with other cellular structures.

In fact, segmentation and tracking of nuclei has been performed successfully in various embryos including mouse post-implantation embryos consisting of ~20,000 cells [39–43]. In addition to biological systems, our method can be applicable to non-living particulate systems. Together, these applications will enable us to evaluate the differences in physical features of not only various living systems, but also non-living ones, providing basic information that will improve our understanding of living systems.

Our *in situ* inferences provide information about mechanical states, or maps, of living systems. Various methods have been developed for measuring or inferring mechanical maps in living systems [17,44,78–81]. Our method is advantageous for obtaining mechanical states in three-dimensional situations with temporal evolution. To understand mechanical states, it is necessary to complementary utilize these methods with various temporal and spatial resolutions.

To understand morphogenetic events, mechanical states and simulations based on those states are essential. Models such as vertex and Cellular Potts models are often utilized, especially for epithelial cells, where the cells are modeled as polygonal or polyhedral shapes with adhesion energy and surface tension [5,51,57]. These models successfully recapitulated various morphogenetic events, including the formation of the mouse blastocyst [51], very early embryogenesis in *C.elegans* [82], and the formation of

cystic structures in kidney [57]. These models often contain non-cellular components such as liquid in cavities and egg shells. However, it is still challenging to measure cellular and non-cellular parameters in three-dimensional systems with high spatiotemporal resolution, although high-resolution inference has been performed in two-dimensional situations [44,81]. This means that there is no clear way to connect the model parameters to *in vivo* ones in three-dimensional systems. On the other hand, particle-based cellular models can also assume parameters other than the potential of cell–cell interactions, leading to recapitulation of complex three-dimensional structures such as the blastocyst [83–85]. In particular, a recent study reported a model that considered cell polarities, in which transformation from cell aggregates to cell sheets and bending of cell sheets were simulated [85]. Particle-based models have also been expanded by considering cell shapes, where a cell is composed of two particles or a Voronoi tessellation is combined to implement multibody effect [22,31–35,56], and mechanical properties and dynamics of self-propelled cells or cell aggregates were investigated. These observations suggest that particle-based models are potentially applicable to very complex structures, although it has not been established whether highly deformed cells and non-cellular structures such as extracellular matrix can be implemented simply in particle-based models. In our strategy, model parameters inferred from *in vivo* systems can be used for simulations.

Our method provides a framework for quantitatively connecting model parameters to *in vivo* parameters under three-dimensional situations, and will thus be complementary to other models.

Investigations of the origins of the effective potentials are important for a complete understanding of morphogenesis. Various proteins including cadherins and actomyosins should be involved in the potentials. In fact, disruption of the gene encoding α-catenin, which is essential for the function of cadherin proteins, leads to the changes in the profile of effective potentials (Fig. S4). Our framework enables us to relate proteins to the profile of potentials by evaluating the effect of gene disruption or inhibition on the profile. Comprehensive evaluation of the effect of various proteins will be valuable, and will provide a bridge between the physics of morphogenesis and molecular biology.

Toward understanding of a later stage of embryogenesis and organogenesis

In this study, we used relatively small embryos: mouse pre-implantation embryos (several tens of cells) and the *C. elegans* embryo (< 350 cells). To apply our inference method and simulation model to later embryonic stages, new components should be considered, such as the increase in the number of cell types, cell polarities,

and chemotaxis. The number of cell types increases through cell differentiation, in which mesenchymal cells as well as blastomere cells and epithelial cells are included. The blastocyst contains at least two cell types (ICM and TE), and we successfully detected the differences in the DF curves between these two cell types (Fig. S6). In later stages of embryogenesis, such as gastrulation, the embryos are usually composed of mixtures, in which the epithelial-to-mesenchymal transition occurs. In contrast to the vertex model, where mesenchymal cells cannot be considered, particle-based models may simulate the mesenchymal cells and mixtures of mesenchymal and epithelial cells [24,25]. Cell sorting of different cell types has been explained by differential cell–cell adhesiveness, and particle-based models can reproduce cell sorting by considering cell–cell adhesiveness as potentials (Fig. S9G) [86]. Apico-basal and planar cell polarities are critical parameters for morphogenesis [85]. We speculate that these polarities can be implemented in the particle model by implementing two particles for a cell [31,32], or by considering directional differences in the profiles of effective potentials, as recently proven by other group [85]. Cell–cell interactions are regulated not only by mechanical forces but also by chemical signaling such as chemotaxis and ephrin proteins (Fig. S1B). By expanding the concept of effective potentials, we think that attractive and repulsive effects of chemical signaling can be implemented as the profile of the effective

potentials, possibly with non-reciprocal interactions [87–90]. It is possible that by analyzing inferred cell–cell interaction forces, we could extract differences in cell types, directional differences in the profile of the effective potentials, and the effects of chemotaxis.

At this moment, we do not know whether the particle-based model is useful for later stages of embryogenesis or larger tissues to which continuum models are usually applied [91]. Multi-scale frameworks may be required to connect particle-based models with continuum models. In any case, our inference method may be useful for evaluating material properties of larger tissues, which are essential for developing continuum models.

Conclusion

Our framework, composed of the inference method and the particle-based model, has various potential uses for investigating the properties of cell–cell interaction, single-cell analysis of mechanics, material properties, mechanical maps, three-dimensional morphogenesis, relationships between mechanical parameters and gene products, and comparisons of mechanical parameters and behaviors among different living species and non-living systems. Although some of these issues will be

examined in the future, we propose that our framework provides a novel physical scenario for understanding the biophysics and physical biology of diverse morphogenetic events.

Experimental materials and methods

Mouse embryos were obtained by mating Rosa26-H2B-EGFP knock-in male mice [43] with ICR female mice. Animal care and experiments were conducted in accordance with the Guidelines of Animal Experiment of the National Institutes of Natural Sciences. Experiments were approved by the Institutional Animal Care and Use Committee of the National Institutes of Natural Sciences. MDCK transgenic cells bearing H2B-EGFP were generated using a piggy-bac plasmid [92,93]. α-catenin mutant cells were constructed previously [94]. The detailed procedures for cell and embryo cultures, microscopic imaging, nuclear tracking, force inference, simulations, and data analyses are described in SI. The nuclear tracking data, inferred forces, and profiles of distance–force curves are provided in SI.

Acknowledgement

We thank Drs. Hitoshi Niwa and Yayoi Toyooka for providing the piggy-bac plasmids and technical suggestions. We thank Drs. Jean-François Joanny, Hiroaki Takagi and Yasuhiro Inoue for critical reading of the manuscript. We thank Dr. Yoshitaka Kimori for helpful discussions. We thank Ms. Azusa Kato for supporting nuclear tracking. This work was supported by following grants: Japan Ministry of Education, Culture, Sports, Science and Technology Grant-in-Aid for Scientific Research on Innovative Areas "Cross-talk between moving cells and microenvironment as a basis of emerging order" for H.K., the National Institutes of Natural Sciences (NINS) program for cross-disciplinary science study for H.K., a Japan Society for the Promotion of Science (JSPS) Grant-in-Aid for Young Scientists (B) for H.K. (17K15131), for Scientific Research (C) for T.O. (18K06234), and for Young Scientists (B) for T.O. (16K18544), a MEXT/JSPS Grant-in-Aid for Scientific Research on Innovative Areas for T.O. (17H05627), the Inamori Foundation for T.O., and the Takeda Science Foundation for T.O.

Conflicts of interest

The authors declare no competing financial interests.

Author contribution

H.K. designed the work, H.K., A.M.I., and H.O. contributed to the conception. H.K. and T.F. designed experiments, T.O. provided experimental materials, and H.K. performed experiments and image processing. H.K. and H.O. designed models, H.K. developed computational algorithms, and H.K. and K.N. statistically analyzed the data. H.K., T.O., H.O., A.M.I., K.N., K.K., and T.F. wrote the manuscript, and all authors contributed to the interpretation of the results.

References

1. Pettitt, B. M. & Rossky, P. J. Alkali halides in water: Ion–solvent correlations and ion–ion potentials of mean force at infinite dilution. *J. Chem. Phys.* **84**, 5836–5844 (1986).
2. Israelachvili, J. N. *Intermolecular and Surface Forces*. (Elsevier Inc., 2011).
3. Steinberg, M. S. Differential adhesion in morphogenesis : a modern view. *Curr. Opin. Genet. Dev.* **17**, 1281–286 (2007).
4. Guillot, C. & Lecuit, T. Mechanics of epithelial tissue homeostasis and morphogenesis. *Science (80-.).* **340**, 1185–9 (2013).

5. Fletcher, A. G., Osterfield, M., Baker, R. E. & Shvartsman, S. Y. Vertex models of epithelial morphogenesis. *Biophys. J.* **106**, 2291–2304 (2014).

6. Maître, J.-L. *et al.* Adhesion Functions in Cell Sorting by Mechanically Coupling the Cortices of Adhering Cells. *Science (80-.).* **338**, 253–256 (2012).

7. Bazellières, E. *et al.* Control of cell–cell forces and collective cell dynamics by the intercellular adhesome. *Nat. Cell Biol.* **17**, 409–420 (2015).

8. Yong, J. *et al.* Spatial distribution of cell–cell and cell–ECM adhesions regulates force balance while maintaining E-cadherin molecular tension in cell pairs. *Mol. Biol. Cell* **26**, 2456–2465 (2015).

9. Manning, M. L., Foty, R. A., Steinberg, M. S. & Schoetz, E.-M. Coaction of intercellular adhesion and cortical tension specifies tissue surface tension. *Proc. Natl. Acad. Sci.* **107**, 12517–12522 (2010).

10. David, R. *et al.* Tissue cohesion and the mechanics of cell rearrangement. *Development* **141**, 3672–3682 (2014).

11. Forgacs, G. & Newman, S. A. *Biological Physics of the Developing Embryo*. (Cambridge University Press, 2005).

12. Ma, X. *et al.* Fibers in the extracellular matrix enable long-range stress transmission between cells. *Biophys. J.* **104**, 1410–1418 (2013).

13. Li, X. *et al.* On the mechanism of long-range orientational order of fibroblasts. *Proc. Natl. Acad. Sci.* **114**, 8974–8979 (2017).

14. Atkins, P., Paula, J. De & Keeler, J. *Atkins' Physical Chemistry*. (Oxford University Press, 2018).

15. Ito, A. M., Takayama, A., Saito, S. & Nakamura, H. Formation and Classification of Amorphous Carbon by Molecular Dynamics Simulation. *Jpn. J. Appl. Phys.* **52**, 01AL04 (2013).

16. Frenkel, D. & Smit, B. *Understanding Molecular Simulation*. (Academic Press, 2002).

17. Merkel, M. & Manning, M. L. Using cell deformation and motion to predict forces and collective behavior in morphogenesis. *Semin. Cell Dev. Biol.* **67**, 161–169 (2017).

18. Weikl, T. R., Asfaw, M., Krobath, H., Bartosz, R. & Lipowsky, R. Adhesion of membranes via receptor–ligand complexes: Domain formation, binding cooperativity, and active processes. *Soft Matter* **5**, 3213–3224 (2009).

19. Drasdo, D., Kree, R. & McCaskill, J. S. Monte Carlo approach to tissue-cell populations. *Phys. Rev. E* **52**, 6635–6657 (1995).

20. Drasdo, D. & Höhme, S. A single-cell-based model of tumor growth in vitro:

monolayers and spheroids. *Phys. Biol.* **2**, 133–147 (2005).

21. Yamao, M., Naoki, H. & Ishii, S. Multi-cellular logistics of collective cell migration. *PLoS One* **6**, (2011).

22. Ranft, J. *et al.* Fluidization of tissues by cell division and apoptosis. *Proc. Natl. Acad. Sci. U. S. A.* **107**, 20863–20868 (2010).

23. Sepúlveda, N. *et al.* Collective Cell Motion in an Epithelial Sheet Can Be Quantitatively Described by a Stochastic Interacting Particle Model. *PLoS Comput. Biol.* **9**, e1002944 (2013).

24. Arboleda-Estudillo, Y. *et al.* Movement Directionality in Collective Migration of Germ Layer Progenitors. *Curr. Biol.* **20**, 161–169 (2010).

25. Szabó, B. *et al.* Phase transition in the collective migration of tissue cells: Experiment and model. *Phys. Rev. E* **74**, 061908 (2006).

26. Kashef, J. & Franz, C. M. Quantitative methods for analyzing cell–cell adhesion in development. *Dev. Biol.* **401**, 165–174 (2015).

27. Cornell, W. D. *et al.* A Second Generation Force Field for the Simulation of Proteins, Nucleic Acids, and Organic Molecules. *J. Am. Chem. Soc.* **117**, 5179–5197 (1995).

28. Brooks, B. R. *et al.* CHARMM: A program for macromolecular energy,

minimization, and dynamics calculations. *J. Comput. Chem.* **4**, 187–217 (1983).

29. Hamada, H. *et al.* Involvement of Delta/Notch signaling in zebrafish adult pigment stripe patterning. *Dev.* **141**, 318–324 (2014).

30. Fuerst, P. G., Koizumi, A., Masland, R. H. & Burgess, R. W. Neurite arborization and mosaic spacing in the mouse retina require DSCAM. *Nature* **451**, 470–474 (2008).

31. Basan, M., Prost, J., Joanny, J.-F. & Elgeti, J. Dissipative particle dynamics simulations for biological tissues: rheology and competition. *Phys. Biol.* **8**, 026014 (2011).

32. Basan, M., Elgeti, J., Hannezo, E., Rappel, W.-J. & Levine, H. Alignment of cellular motility forces with tissue flow as a mechanism for efficient wound healing. *Proc. Natl. Acad. Sci.* **110**, 2452–2459 (2013).

33. Bi, D., Yang, X., Marchetti, M. C. & Manning, M. L. Motility-driven glass and jamming transitions in biological tissues. *Phys. Rev. X* **6**, 021011 (2016).

34. Vitorino, P., Hammer, M., Kim, J. & Meyer, T. A Steering Model of Endothelial Sheet Migration Recapitulates Monolayer Integrity and Directed Collective Migration. *Mol. Cell. Biol.* **31**, 342–350 (2011).

35. Honda, H. Description of cellular patterns by Dirichlet domains: The

two-dimensional case. *J. Theor. Biol.* **72**, 523–530 (1978).

36. Garcia, S. *et al.* Physics of active jamming during collective cellular motion in a monolayer. *Proc. Natl. Acad. Sci. U. S. A.* **112**, 15314–15319 (2015).

37. Schötz, E. *et al.* Quantitative differences in tissue surface tension influence zebrafish germ layer positioning. *HFSP J.* **2**, 42–56 (2008).

38. He, B., Doubrovinski, K., Polyakov, O. & Wieschaus, E. Apical constriction drives tissue-scale hydrodynamic flow to mediate cell elongation. *Nature* **508**, 392–396 (2014).

39. Bao, Z. *et al.* Automated cell lineage tracing in Caenorhabditis elegans. *Proc. Natl. Acad. Sci. U. S. A.* **103**, 2707–2712 (2006).

40. McDole, K. *et al.* In Toto Imaging and Reconstruction of Post-Implantation Mouse Development at the Single-Cell Level. *Cell* **175**, 859-876.e33 (2018).

41. Amat, F. & Keller, P. J. Towards comprehensive cell lineage reconstructions in complex organisms using light-sheet microscopy. *Dev. Growth Differ.* **55**, 563–578 (2013).

42. Kyoda, K. *et al.* WDDD: Worm developmental dynamics database. *Nucleic Acids Res.* **41**, D732-7 (2013).

43. Kurotaki, Y., Hatta, K., Nakao, K., Nabeshima, Y.-I. & Fujimori, T. Blastocyst

axis is specified independently of early cell lineage but aligns with the ZP shape. *Science* **316**, 719–23 (2007).

44. Ishihara, S. & Sugimura, K. Bayesian inference of force dynamics during morphogenesis. *J. Theor. Biol.* **313**, 201–211 (2012).

45. Fletcher, S. J. *Data Assimilation for the Geosciences: From Theory to Application*. (Elsevier, 2017).

46. Hirano, S., Kimoto, N., Shimoyama, Y., Hirohashi, S. & Takeichi, M. Identification of a Neural a-Catenin as a Key Regulator of Cadherin Function and Multicellular Organization. *Cell* **70**, 293–301 (1992).

47. Arata, Y., Takagi, H., Sako, Y. & Sawa, H. Power law relationship between cell cycle duration and cell volume in the early embryonic development of Caenorhabditis elegans. *Front. Physiol.* **5**, 529 (2015).

48. Motosugi, N., Bauer, T., Polanski, Z., Solter, D. & Hiiragi, T. Polarity of the mouse embryo is established at blastocyst and is not prepatterned. *Genes Dev.* **19**, 1081–1092 (2005).

49. Fierro-González, J. C., White, M. D., Silva, J. C. & Plachta, N. Cadherin-dependent filopodia control preimplantation embryo compaction. *Nat. Cell Biol.* **15**, 1424–33 (2013).

50. Wang, A. Z., Ojakian, G. K. & Nelson, W. J. Steps in the morphogenesis of a polarized epithelium. *J. Cell Sci.* **95**, 137–152 (1990).

51. Honda, H., Motosugi, N., Nagai, T., Tanemura, M. & Hiiragi, T. Computer simulation of emerging asymmetry in the mouse blastocyst. *Development* **135**, 1407–1414 (2008).

52. Eiraku, M. *et al.* Self-organizing optic-cup morphogenesis in three-dimensional culture. *Nature* **472**, 51–6 (2011).

53. Marmottant, P. *et al.* The role of fluctuations and stress on the effective viscosity of cell aggregates. *Proc Natl Acad Sci U S A* **106**, 17271–17272 (2009).

54. Campàs, O. *et al.* Quantifying cell-generated mechanical forces within living embryonic tissues. *Nat. Methods* **11**, 183–9 (2014).

55. Pérez-González, C. *et al.* Active wetting of epithelial tissues. *Nat. Phys.* **15**, 79–88 (2019).

56. Montel, F. *et al.* Stress Clamp Experiments on Multicellular Tumor Spheroids. *Phys. Rev. Lett.* **107**, 188102 (2011).

57. Belmonte, J. M. *et al.* Virtual-tissue computer simulations define the roles of cell adhesion and proliferation in the onset of kidney cystic disease. *Mol. Biol. Cell* **27**, 3673–3685 (2016).

58. Kessler, M. *et al.* The Notch and Wnt pathways regulate stemness and differentiation in human fallopian tube organoids. *Nat. Commun.* **6**, 8989 (2015).

59. Rivron, N. C. *et al.* Blastocyst-like structures generated solely from stem cells. *Nature* **557**, 106–111 (2018).

60. Aigouy, B. *et al.* Cell Flow Reorients the Axis of Planar Polarity in the Wing Epithelium of Drosophila. *Cell* **142**, 773–786 (2010).

61. Drasdo, D. & Forgacs, G. Modeling the interplay of generic and genetic mechanisms in cleavage, blastulation, and gastrulation. *Dev. Dyn.* **219**, 182–191 (2000).

62. Smutny, M. *et al.* Friction forces position the neural anlage. *Nat. Cell Biol.* **19**, 306–317 (2017).

63. Montesano, R., Schaller, G. & Orci, L. Induction of epithelial tubular morphogenesis in vitro by fibroblast-derived soluble factors. *Cell* **66**, 697–711 (1991).

64. Atsuta, Y. & Takahashi, Y. FGF8 coordinates tissue elongation and cell epithelialization during early kidney tubulogenesis. *Development* **142**, 2329–2337 (2015).

65. Koyama, H. *et al.* Mechanical Regulation of Three-Dimensional Epithelial Fold

Pattern Formation in the Mouse Oviduct. *Biophys. J.* **111**, 650–665 (2016).

66. Serra, D. *et al.* Self-organization and symmetry breaking in intestinal organoid development. *Nature* **569**, 66–72 (2019).

67. Solnica-krezel, L. & Sepich, D. S. Gastrulation: Making and Shaping Germ Layers. *Annu. Rev. Cell Dev. Biol.* **28**, 687–717 (2012).

68. Moriwaki, K., Tsukita, S. & Furuse, M. Tight junctions containing claudin 4 and 6 are essential for blastocyst formation in preimplantation mouse embryos. *Dev Biol* **312**, 509–22 (2007).

69. Wang, X. *et al.* Characterizing Inner Pressure and Stiffness of Trophoblast and Inner Cell Mass of Blastocysts. *Biophys. J.* **115**, 2443–2450 (2018).

70. Dumortier, J. G. *et al.* Hydraulic fracturing and active coarsening position the lumen of the mouse blastocyst. *Science (80-.).* **365**, 465–468 (2019).

71. Orsogna, M. R. D., Chuang, Y. L., Bertozzi, A. L. & Chayes, L. S. Self-Propelled Particles with Soft-Core Interactions : Patterns , Stability , and Collapse. *Phys. Rev. Lett.* **96**, 104302 (2006).

72. Delile, J., Herrmann, M., Peyriéras, N. & Doursat, R. A cell-based computational model of early embryogenesis coupling mechanical behaviour and gene regulation. *Nat. Commun.* **8**, 13929 (2017).

73. Shimoyama, N., Sugawara, K., Mizuguchi, T., Hayakawa, Y. & Sano, M. Collective Motion in a System of Motile Elements. *Phys. Rev. Lett.* **76**, 3870–3873 (1996).

74. Helbing, D. & Molnár, P. Social force model for pedestrian dynamics. *Phys. Rev. E* **51**, 4282–4286 (1995).

75. Couzin, I. D. & Krause, J. Self-Organization and Collective Behavior in Vertebrates. *Adv. study Behav.* **32**, 1–75 (2003).

76. Sugi, T., Ito, H., Nishimura, M. & Nagai, K. H. C. elegans collectively forms dynamical networks. *Nat. Commun.* **10**, 683 (2019).

77. Azuma, Y. & Onami, S. Biologically constrained optimization based cell membrane segmentation in C . elegans embryos. *BMC Bioinformatics* **18**, 307 (2017).

78. Campàs, O. A toolbox to explore the mechanics of living embryonic tissues. *Semin. Cell Dev. Biol.* **55**, 119–130 (2016).

79. Serwane, F. *et al.* In vivo quantification of spatially varying mechanical properties in developing tissues. *Nat. Methods* **14**, 181–186 (2017).

80. Scarcelli, G. *et al.* Noncontact three-dimensional mapping of intracellular hydromechanical properties by Brillouin microscopy. *Nat. Methods* **12**, 1132–

1134 (2015).

81. Tambe, D. T. *et al.* Collective cell guidance by cooperative intercellular forces. *Nat. Mater.* **10**, 469–75 (2011).

82. Kajita, A., Yamamura, M. & Kohara, Y. Computer simulation of the cellular arrangement using physical model in early cleavage of the nematode Caenorhabditis elegans. *Bioinformatics* **19**, 704–716 (2003).

83. Krupinski, P., Chickarmane, V. & Peterson, C. Simulating the Mammalian Blastocyst - Molecular and Mechanical Interactions Pattern the Embryo. *PLoS Comput. Biol.* **7**, e1001128 (2011).

84. Nissen, S. B. *et al.* Four simple rules that are sufficient to generate the mammalian blastocyst. *PLoS Biol.* **15**, e2000737 (2017).

85. Nissen, S. B., Rønhild, S., Trusina, A. & Sneppen, K. Theoretical tool bridging cell polarities with development of robust morphologies. *Elife* **7**, e38407 (2018).

86. Belmonte, J. M., Thomas, G. L., Brunnet, L. G., de Almeida, R. M. C. & Chate, H. Self-Propelled Particle Model for Cell-Sorting Phenomena. *Phys. Rev. Lett.* **100**, 248702 (2008).

87. Mammoto, T. *et al.* Mechanochemical Control of Mesenchymal Condensation and Embryonic Tooth Organ Formation. *Dev. Cell* **21**, 758–769 (2011).

88. Yamanaka, H. & Kondo, S. In vitro analysis suggests that difference in cell movement during direct interaction can generate various pigment patterns in vivo. *Proc. Natl. Acad. Sci.* **111**, 1867–1872 (2014).

89. Kano, T., Osuka, K., Kawakatsu, T. & Ishiguro, A. Mathematical Analysis for Non-reciprocal-interaction-based Model of Collective Behavior. *J. Phys. Soc. Japan* **86**, 124004 (2017).

90. Rodriguez-Franco, P. *et al.* Long-lived force patterns and deformation waves at repulsive epithelial boundaries. *Nat. Mater.* **16**, 1029–1036 (2017).

91. Shyer, A. E. *et al.* Villification: how the gut gets its villi. *Science* **342**, 212–8 (2013).

92. Nakatake, Y. *et al.* Kinetics of drug selection systems in mouse embryonic stem cells. *BMC Biotechnol.* **13**, (2013).

93. Guo, G. *et al.* Klf4 reverts developmentally programmed restriction of ground state pluripotency. *Development* **136**, 1063–1069 (2009).

94. Otani, T. *et al.* Claudins and JAM-A coordinately regulate tight junction formation and epithelial polarity. *J. Cell Biol.* (2019). doi:10.1083/jcb.201812157

Figures

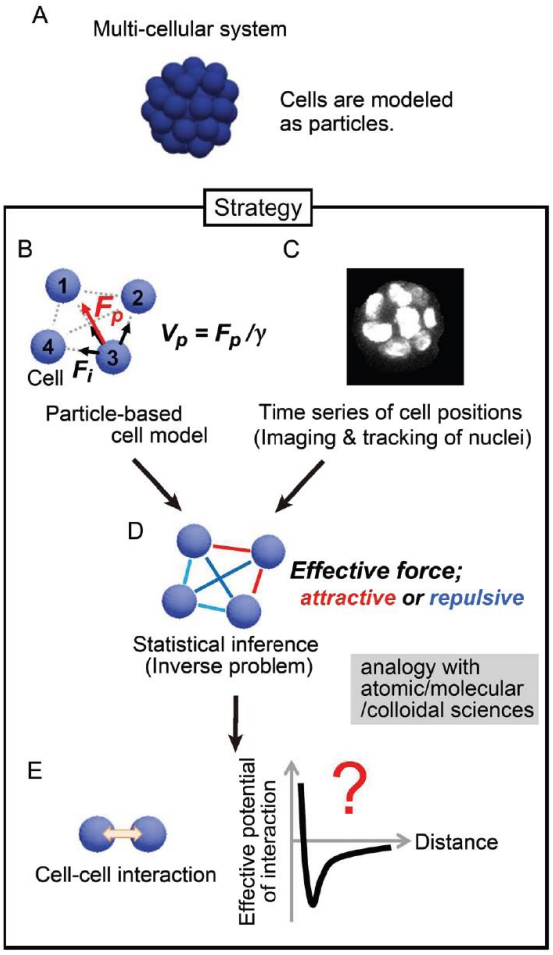

Figure 1: Overview of strategy for inferring the effective potential of cell–cell interactions

A. Cells were modeled as particles. A blue sphere corresponds to a cell. B. In the particle-based cellular model, attractive or repulsive force between the particles (blue spheres #1–4), was considered; force vectors (F_i) are illustrated by black arrows in the case of particle #3. The net force (F_p) is shown by a red vector, and the relationship

between F_p and velocity (V_p) is described. C. From a time series of microscopic images of nuclei, nuclear tracking data were obtained. An image derived from a cyst formed by MDCK cells expressing H2B-EGFP is shown as an example. D. Effective forces of cell–cell interactions were inferred by solving an inverse problem: we statistically searched for force values in the model (B) that could reproduce the nuclear tracking data (C). E. The inferred force values (D) were plotted against the distance between cell–cell interactions, and the plots were examined for emergence of distance–force or –potential curves.

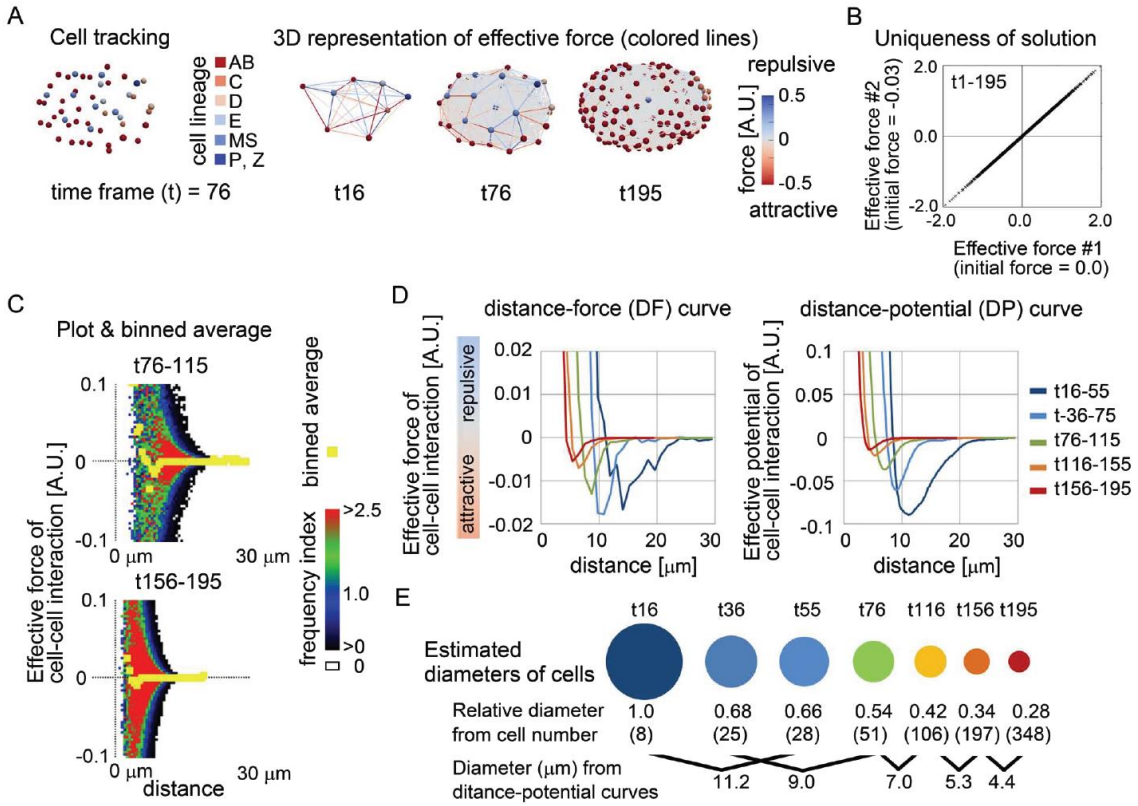

Figure 2: Inference of effective force of cell–cell interaction in *C.elegans* embryos

A. Snapshot of the nuclear positions in the *C.elegans* embryo (left panel) and snapshots with inferred effective forces (right three panels) were three-dimensionally visualized at the time frames as described (t16, t76, and t195); the interval between time frames is 1 min. The spheres correspond to cells whose colors represent cell lineages, including AB, C, D, E, MS, and P & Z. The lines represent cell–cell interactions; the colors indicate the values of the effective forces (red, attractive; blue, repulsive). Forces are depicted in arbitrary units (A.U.); 1 A.U. of the force can move a particle at 1μm/min as described in SI (Section 3-4). The nuclear tracking data were obtained from a previous report [39].

Related figures and movies are provided (Fig. S5A, B, Movies S3A and B). B. Uniqueness of solution of effective force inference was examined. The minimizations of Equation 5 were performed from different initial force values as described in the x- and y- axes, and the inferred values of each cell-cell interaction were plotted by crosses. The inferred values from the different initial force values were absolutely correlated. Values from all time frames (t1-195) were applied. C. The inferred effective forces of cell–cell interaction were plotted against the distance of the cell–cell interaction. The graph space was divided into 64×64 square regions, and the frequencies of the data points plotted in each region were calculated. The mean value of the frequencies was calculated for each of the 64 columnar regions along the distance. Frequency index (FI) is defined so that the mean value of the frequencies is 1, and a colored heat map was generated according to the FI. White corresponds to an FI of 0. Averaged values of the forces were calculated for 64 columnar regions along the distance, and are shown in yellow (binned average). Detailed procedures are described in SI (Section 4). The graphs for time frame 76–115 and 156–195 are shown. Data at other time frames are provided in Figure S5C. D. Distance–force and distance–potential curves were estimated. The averaged values of the effective forces in (C) were smoothed over the distance, and the potentials were calculated by integrating the forces. Details are described in SI (Section 4). The curves

for each time frame are shown. E. Mean diameters of cells at each time frame were estimated from cell numbers and the distance–potential curves. Given that the volume of the embryos is constant (= Vol) during embryogenesis, the mean diameters were estimated from the cell numbers (N_c) at each time frame as follows: mean diameter = $\{Vol / (4/3\ \pi\ N_c)\}^{1/3}$. The diameters relative to that at time frame = 16 are shown with cell numbers (parentheses). The sizes of the circles reflect the diameters, whose colors roughly correspond to the colors in the graph in D. The diameters were also estimated from the distance–potential curves in D; the distances with minima of the distance–potential curves roughly reflect the diameters (Fig. S2D).

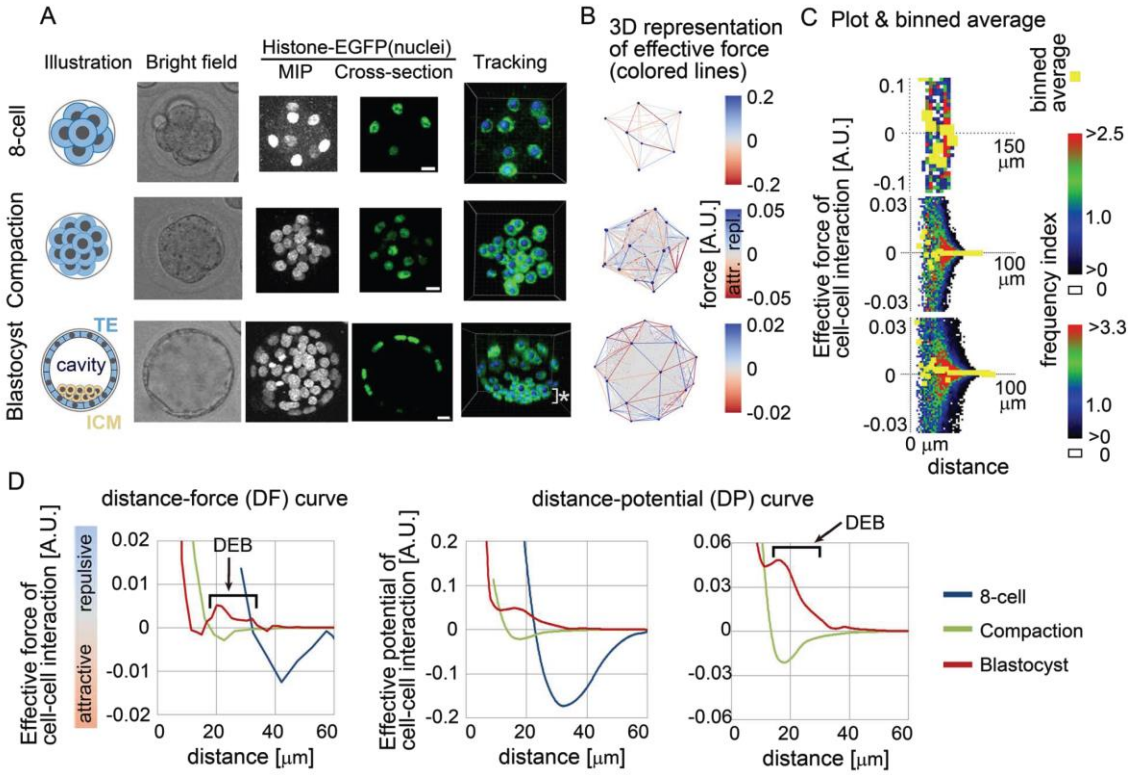

Figure 3: Inference of the effective force of cell–cell interaction in mouse pre-implantation embryos

A. Eight-cell, compaction, and blastocyst stages of mouse embryo are illustrated, and their confocal microscopic images are shown: bright field, maximum intensity projection (MIP) and cross-section of fluorescence of H2B-EGFP. Snapshots of nuclear tracking are also shown; blue spheres indicate the detected nuclei. In the illustration of the blastocyst, ICM and TE cells are depicted by orange and blue, respectively, and a cavity is also described. In the nuclear tracking image of the blastocyst, ICM cells are located around the bottom region of the image, as indicated by *. Scale bars = 15µm.

Related movies are provided (Movie S4A–C). B. Snapshots of nuclear positions with inferred effective forces were visualized three-dimensionally for the three embryonic stages in a manner similar to Figure 2A. Blue spheres correspond to cells. The lines represent cell–cell interactions, and the colors indicate the values of the effective forces [red, attractive (attr.); blue, repulsive (repl.)]. Related movies are provided (Movie S4D-G). The uniqueness of the solutions was confirmed in Figure S7B. C. The inferred effective forces of cell–cell interactions were plotted against the distance of cell–cell interactions in a manner similar to Figure 2C, except that the graph space of the 8-cell stage was divided into 32×32 square regions, and the averaged values were calculated for the 32 columnar regions. D. Distance–force and distance–potential curves were estimated from (C) in a manner similar to Figure 2D. A distant energy barrier (DEB) was detected, as indicated by arrows. Data from other embryos are provided in Figure S5D. The differences in distance–force and distance–potential curves between ICM and TE cells and between the outer and inner cells in the compaction state were described in Figure S6.

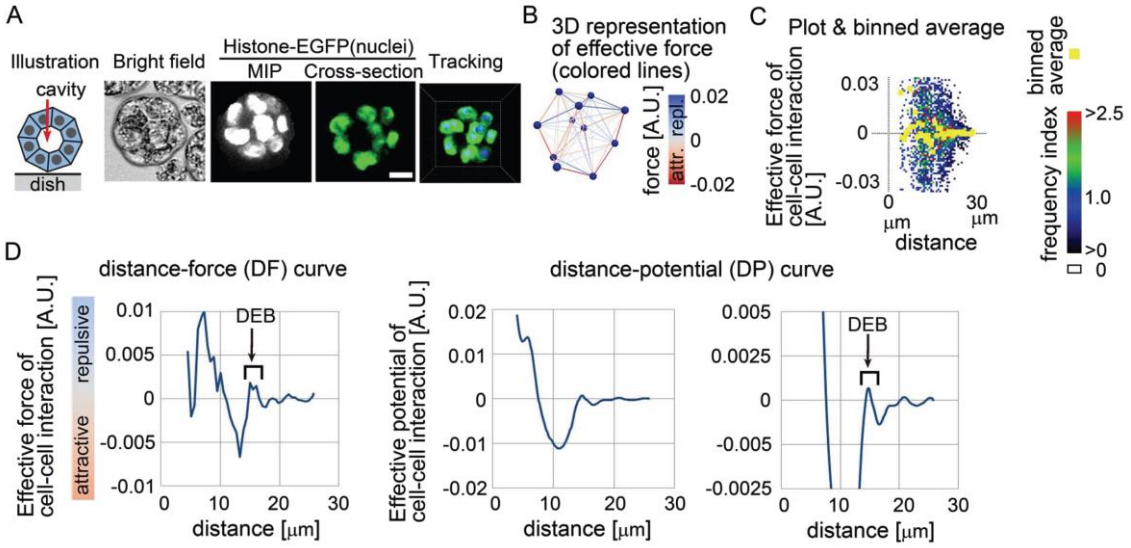

Figure 4: Inference of effective force of cell–cell interaction in cysts formed by MDCK cells

A. MDCK cysts formed under suspension conditions are illustrated, and confocal microscopic images are shown: bright field, maximum intensity projection (MIP) and cross-section of fluorescence of H2B-EGFP. A snapshot of nuclear tracking is also shown; blue spheres represent nuclei. Scale bars = 10μm. A related movie is provided (Movie S5A). B. A snapshot of the nuclear positions with inferred effective forces was three-dimensionally visualized in a manner similar to Figure 2A. The blue spheres correspond to cells. The lines represent cell–cell interactions and the colors indicate the values of the effective forces [red, attractive (attr.); blue, repulsive (repl.)]. A related movie is provided (Movie S5B). The uniqueness of the solutions was confirmed in

Figure S7C. C. The inferred effective forces of cell–cell interaction were plotted against the distance of cell–cell interaction in a manner similar to Figure 2C. D. Distance–force and distance–potential curves were estimated from (C) in a manner similar to Figure 2D. DEB was detected as indicated by arrows. Data from other cysts are provided in Figure S5E.

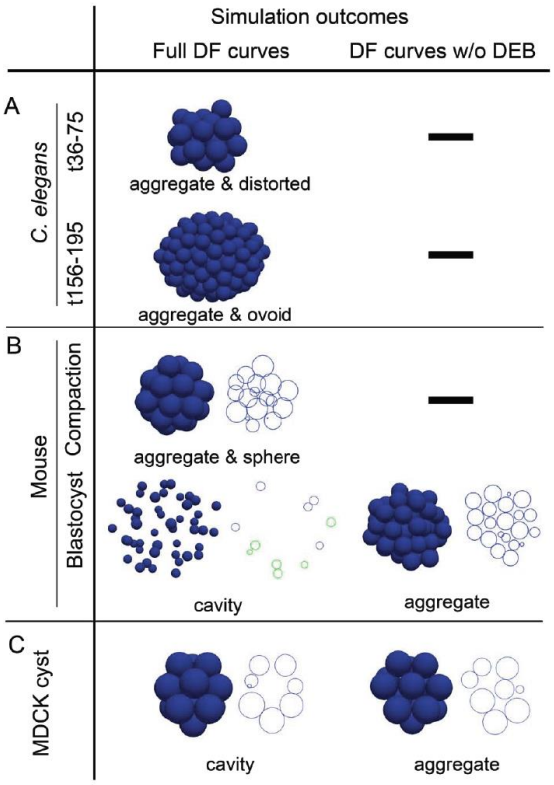

Figure 5: Outcomes of simulations based on inferred distance–force curves

Simulations results under the DF curves derived from *C. elegans* (A) and mouse embryos (B), and the MDCK cyst (C) are shown. Blue spheres correspond to cells. In the *C. elegans* embryos, the DF curves were derived from time frames 36–75 and 156–195 in Figure 2D. In the mouse embryos, the DF curves were derived from the compaction and blastocyst stages in Figure 3D. Cross-sections are also visualized. In the case of the mouse blastocyst, two parallel cross-sections (shown in blue and green) are merged. In the MDCK cyst, the DF curves are derived from Figure 4D. In the blastocyst and the MDCK cyst, the DF curves without DEB were also applied (w/o

DEB). The diameters of the blue spheres are set to be equivalent to the distance with the minimum potential (Fig. S2D). The initial configurations of the simulations are described in Figure S8, along with other simulation results.

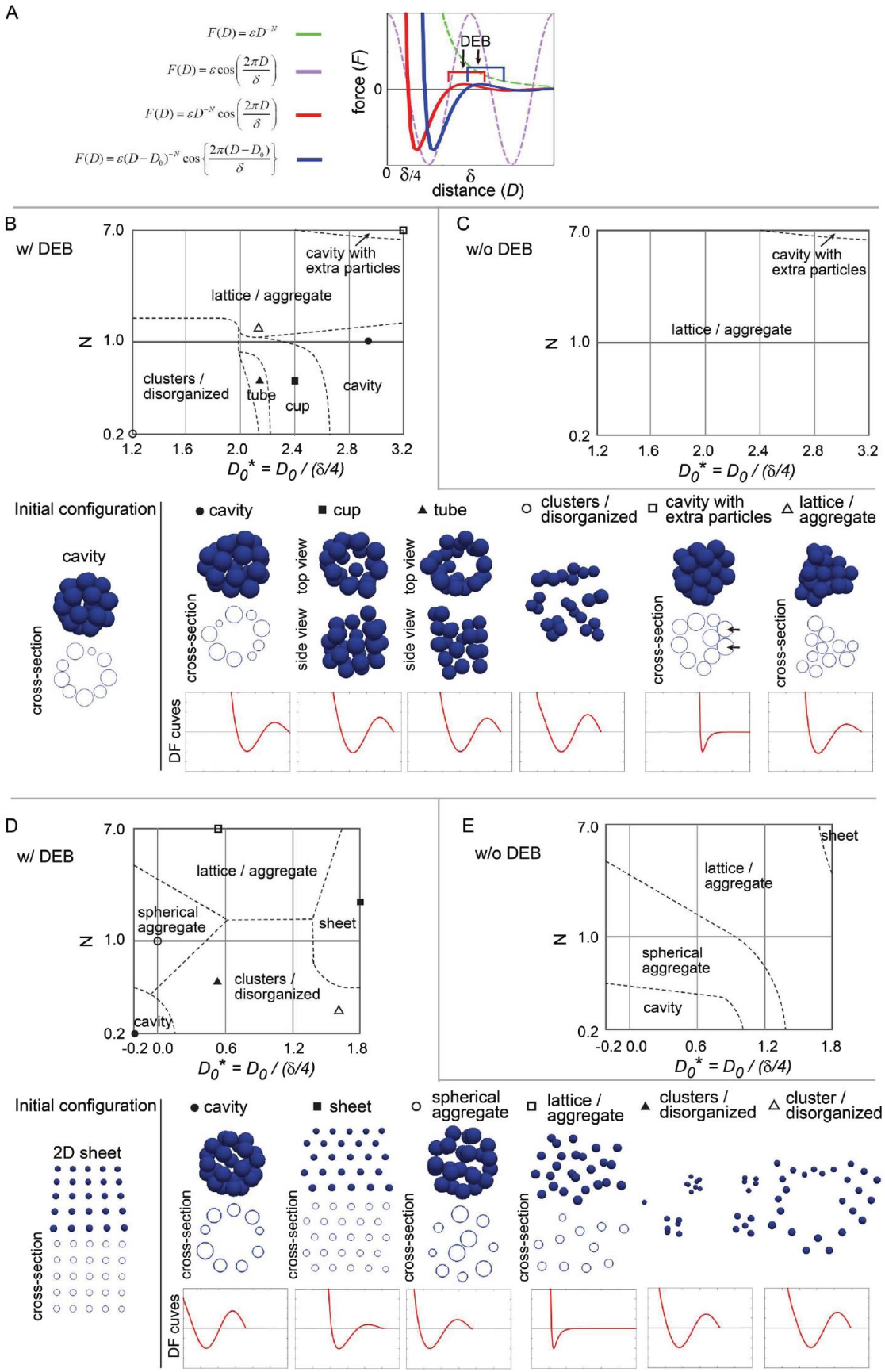
A
$F(D) = \varepsilon D^{-N}$
$F(D) = \varepsilon \cos\left(\frac{2\pi D}{\delta}\right)$
$F(D) = \varepsilon D^{-N} \cos\left(\frac{2\pi D}{\delta}\right)$
$F(D) = \varepsilon (D - D_0)^{-N} \cos\left\{\frac{2\pi (D - D_0)}{\delta}\right\}$
DEB
force (F)
0
0 δ/4 δ
distance (D)
B
w/ DEB
cavity with extra particles
lattice / aggregate
clusters / disorganized
tube
cup
cavity
N
$D_0^* = D_0 / (\delta/4)$
C
w/o DEB
cavity with extra particles
lattice / aggregate
Initial configuration
cavity
cross-section
● cavity
■ cup
▲ tube
○ clusters / disorganized
□ cavity with extra particles
△ lattice / aggregate
top view
side view
DF cuves
D
w/ DEB
lattice / aggregate
spherical aggregate
sheet
clusters / disorganized
cavity
E
w/o DEB
sheet
lattice / aggregate
spherical aggregate
cavity
Initial configuration
2D sheet
● cavity
■ sheet
○ spherical aggregate
□ lattice / aggregate
▲ clusters / disorganized
△ cluster / disorganized

1092

Figure 6: Modeling of distance–force curves and diagrams of simulation outcomes

A. DF curves were mathematically modeled using four variables: N, D_0, δ, and ε. In the case of the DF curves without the cosine term, the curves ($F = \varepsilon\,(D - D_0)^{-N}$) are always >0 (repulsive) and gradually approach 0 as D increases (green broken line). Upon introduction of the cosine (purple broken line), the curves aquire regions with <0 (attractive) and DEB (red line). Upon introduction of D_0, the curves are translated along the distance (blue line). DF curves from D = 0 to D at the end of DEB (w/ DEB) or the curves from D = 0 to D before starting DEB (w/o DEB) were used in the following simulations. The physical meaning and interpretation of these variables are described in SI, Section 5. B. Simulations were performed starting from an initial configuration, and the outcomes under various values of N and D^* are shown in the diagrams. A cavity-bearing structure was given as the initial configuration; the blue spheres correspond to cells, and a cross-section is visualized. According to the conditions, a cavity was maintained, whereas cups, tubes, etc. were generated. Some conditions on the diagram were designated by symbols (circle, square, and triangle), and their simulation results are visualized (blue spheres). Example profiles of the DF curves are shown. The diameters of the blue spheres are set to be 0.5× the distance with the

minimum potential, which corresponds to the distance with $F = 0$ (arrows in the profiles of the DF curves, Fig. S2D). In the case of the cavity with extra particles, the extra particles are shown by arrows. C. Simulation outcomes are shown on diagrams similar to B, except that the simulations were performed without DEBs. D. Similar to B, except that the initial configuration was a two-dimensional sheet with slight positional fluctuations According to the conditions, the two-dimensional sheet was maintained, whereas aggregates, cavities etc. were generated. The diameters of the blue spheres are set to be 0.2× the distance with the potential minimum. E. Similar to D, except that the simulations were performed without DEBs. Other diagrams are provided in Figure S9A–E.

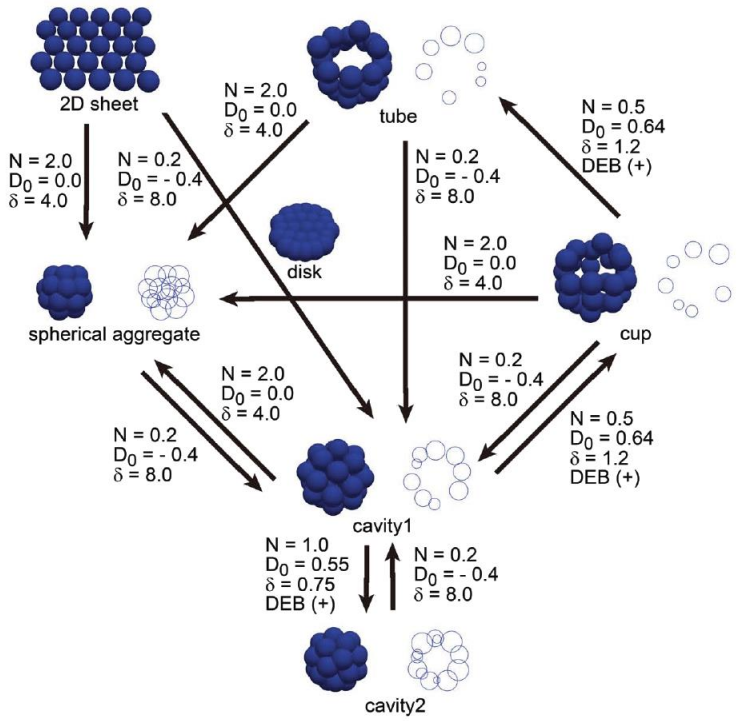

Figure 7: Morphological transitions achieved by distance–force curves

Possible morphological transitions that can be achieved by modulating the values of three variables: N, D_0, and δ in Figure 6. The values of the variables are presented. Conditions with DEB are indicated as DEB (+). The analysis focused on specific structures: cavity-bearing structures, cup, tube, spherical aggregate, two-dimensional sheet, and disk. The cup is a transition state from the cavity-bearing structure to the tube. The disk is also a transition state from the two-dimensional sheet to the cavity-bearing structure. A related movie is provided (Movie S6).